

AperTO - Archivio Istituzionale Open Access dell'Università di Torino

Zeolite morphology and catalyst performance: conversion of methanol to hydrocarbons over offretite

This is the author's manuscript

Original Citation:

Availability:

This version is available <http://hdl.handle.net/2318/1659452> since 2018-02-02T10:24:52Z

Published version:

DOI:10.1039/C7CY00996H

Terms of use:

Open Access

Anyone can freely access the full text of works made available as "Open Access". Works made available under a Creative Commons license can be used according to the terms and conditions of said license. Use of all other works requires consent of the right holder (author or publisher) if not exempted from copyright protection by the applicable law.

(Article begins on next page)



UNIVERSITÀ DEGLI STUDI DI TORINO

This is an author version of the contribution published on:

Questa è la versione dell'autore dell'opera:

[Catalysis Science & Technology, 7, 2017, DOI: 10.1039/c7cy00996h]

The definitive version is available at:

La versione definitiva è disponibile alla URL:

[<http://pubs.rsc.org/en/content/articlelanding/2017/cy/c7cy00996h#!divAbstract>]

Zeolite morphology and catalyst performance: Conversion of methanol to hydrocarbons over offretite

Katarzyna Anna Łukaszuk,^{a,b} Daniel Rojo-Gama,^{a,b} Sigurd Øien-Ødegaard,^a Andrea Lazzarini,^a Gloria Berlier,^c Silvia Bordiga,^c Karl Petter Lillerud,^a Unni Olsbye,^a Pablo Beato,^b Lars Fahl Lundegaard,^{b,*} Stian Svelle^{b,*}

*Corresponding authors

^aDepartment of Chemistry, University of Oslo, P.O. Box 1033 Blindern, N-0315 Oslo, Norway

^bHaldor Topsøe A/S, Haldor Topsøes Allé 1, DK-2800 Lyngby, Denmark

^cDepartment of Chemistry, University of Turin, via Quarellotto 15, I-10135 Turin, Italy

*Corresponding authors:

Stian Svelle: e-mail: stian.svelle@kjemi.uio.no

Lars Fahl Lundegaard: e-mail: lafl@topsoe.dk

Abstract

The synthesis, characterization and catalytic performance of offretite with four distinct crystal morphologies (oval, hexagonal, broccoli-like, spherical) are presented. As a member of the ABC-6 family of zeolite structures, offretite is likely to form intergrowths which can affect shape-selective properties. Herein, the combination of experiments (SC-XRD, PXRD, benzene uptake and the methanol-to-hydrocarbon conversion) allow the determination of the mechanism and fraction of twinning. It is demonstrated that the catalysts with the same crystal aspect ratio (AR=3) yield product spectra dominated by C₂-C₄ aliphatics. Such product selectivity is associated with zeolites with 8-ring channel system. Interestingly, a significant production of bulky aromatics is seen for the catalyst with spherical morphology (AS=1.1) which is a manifestation of the 12-ring pore system of the OFF framework topology. This constitutes the first report of this behavior. The particular display of product shape selectivity can be ascribed to the catalyst particle morphology.



Introduction

Zeolites are fascinating materials with unique properties which find widespread use in chemical industry. The crystalline aluminosilicates have pores or channels of molecular dimensions, and the active sites are dispersed within these pores, giving rise to shape selectivity. It is well known that the performance of zeolites as heterogeneous catalysts is greatly influenced by framework topology and acidity; both the strength and density of acid sites. The crystal size and shape are two further parameters that have been shown to affect catalytic functionality¹ controlling the length of the channels by changing e.g. the size and/or morphology of the crystals, it is possible to decrease or increase the length of the diffusion paths. In consequence, it is possible for example to diminish the propensity for coke formation inside the channels and cages that ultimately is responsible for catalyst deactivation.

Thus, it becomes clear that crystal morphology could constitute a parameter for tuning the properties of zeolite catalysts². This option is little explored, primarily due to major synthesis challenges. Other relevant issues are how the faces are related to the crystal structure and ultimately the pore system, the size and shape of these facets, the overall crystal size, and the crystal aspect ratio. Given the complexity, it is of relevance to introduce and discuss these issues in order to understand their influence on the catalytic performance, which is studied and discussed in this contribution.

Figure 1 was created to illustrate the necessary parameters needed to describe the general morphology of an offretite crystal. The overall size of the crystal is reflected in the absolute values of L and W, where L is the dimension along the unique c-axis and W is the dimension in the orthogonal direction. The aspect ratio (AR) defined as L/W is a supportive information to describe crystal morphology. In cases where $L < W$ the morphology is described as plates, and in cases where $L > W$ it is described as prismatic. In the extreme case where L is completely dominating ($L \gg W$) the crystals are described as needles.

For 1D channel systems in particular, small ARs become desirable due to the short diffusion pathways. Clearly, such materials would provide an increased sorbate access to the active sites within a crystal and would presumably not be affected by coking to the same extent as for crystals with higher AR. It may be noted that the aspect ratios of crystals having different sizes but the same shape will be equal.

The external form of a crystal is the result of the crystal growth. Crystals often adopt external geometrical forms reflecting the symmetries involved in their structures. For example, crystals having a structure which belongs to hexagonal space group can grow to form hexagonal shapes. However, the crystal habit of synthesized materials often differs from the predicted regular polygons, as the morphology is not only defined by the internal factor (structure). It is also related to external factors such as the crystal growth conditions, which may result in crystallization into irregular geometric forms. An understanding of how the morphology of a crystal is determined by the combined effects of structure and synthesis conditions could allow us to tailor make materials with properties targeted for specific applications.

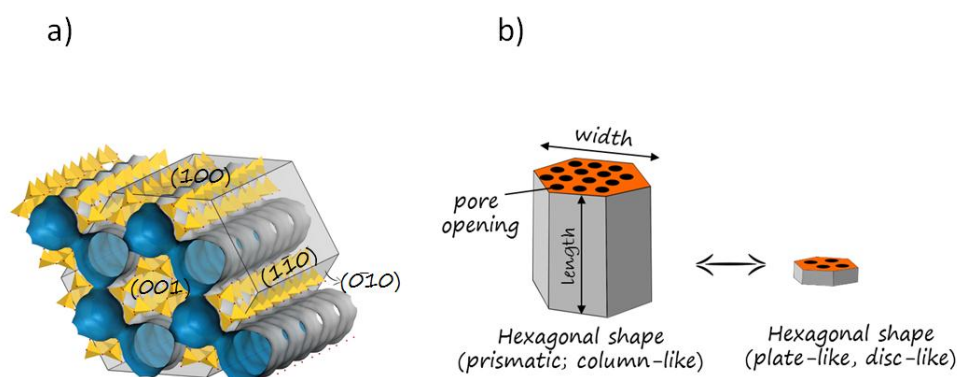


Figure 1. (A) The pore system in the hexagonal offretite crystal in blue (inside of pores) and grey (outside of pores). The outlined prismatic morphology was simulated using the Bravais-Friedel-Donnay-Harker (BFDH) method. (B) Examples of different hexagonal crystal shapes.

The objective of this work is to further study our previously described concept of morphology induced shape selectivity³. This concept recognizes that the unique catalytic behavior of zeolites can be significantly modulated by changes in the crystal shape. Consider a zeolite having two distinct pore systems with different properties (or sizes) that terminate or are exposed on different crystal facets. In such a scenario, one can effectively control the product distribution, in a product shape selective catalytic reaction, by tuning the fraction of pore openings exposed on the external crystal surface via manipulation of the morphology³.

In the current study, the conversion of methanol to hydrocarbons is investigated. This is both due to the industrial relevance of this reaction and because the product spectrum is strongly influenced by product shape selectivity^{4, 5}. The MTH process thereby constitutes an excellent test reaction to probe the fundamental influence of morphology on catalyst performance. Zeolite offretite (OFF) was used as a model catalyst because its pore system consists of straight 12-ring channels interconnected by perpendicular sinusoidal 8-ring channels (**Figure 1a**).

It is well known that offretite is not an efficient catalyst for this reaction. Several early studies of the methanol to hydrocarbons reaction describe the catalytic performance of offretite or related catalysts. Dejaifve *et al.*⁶ studied the reaction over H-offretite (Si/Al = 4.0) at 377 °C and WHSV = 10 h⁻¹ and report an initial conversion of less than 100%. The time required to reach full deactivation was ~1 h, with a high selectivity to coke (10 C%). Detailed product selectivities were not reported⁶. Kanazirev and Tsoncheva⁷ followed the methanol conversion over H-offretite (Si/Al = 4.5; prepared using tetramethyl ammonium) at moderate reaction temperatures (244 °C), primarily focusing on autocatalysis. Low conversion was reported and C₁ to C₃ were the only reported gas phase hydrocarbon products. Offretite-erionite intergrowths (zeolite T) appear to have been studied in more detail. Langner⁸ investigated a zeolite T catalyst (Si/Al = 3.3) at 300 and 400 °C and found a product rich in light aliphatics with a negligible production of C₅₊ products at either reaction temperature. The catalyst lifetime was moderate and the selectivity to coke high (10-12 C%). Clearly, the high selectivity towards the lower linear olefins are a result of the dominant contribution from the erionite structure to the shape selectivity for such intergrown materials⁸. A similar observation was made by Ceckiewicz⁹ using several zeolite T catalysts with varying degree of cation exchange. Ceckiewicz reports also substantial methane formation⁹. Anderson *et al.*¹⁰ compared offretite (prepared using tetramethyl ammonium), ZSM-34 (erionite/offretite intergrowth obtained using choline chloride), and two intermediate erionite/offretite intergrowths (mixed structure directing agent), using primarily solid state NMR. Again, it

was found that the erionite dominated materials were fairly selective towards ethene and propene. In contrast, highly branched long chain polymeric hydrocarbons were detected inside deactivated offretite catalysts, and this was linked to the space offered by the comparatively open 12 ring channels of this material¹⁰. Of particular interest is the work of Occelli *et al.*^{11, 12} Six materials of varying degree of offretite/erionite intergrowths were carefully characterized using among other methods electron microscopy, and it was demonstrated that the selectivity towards ethene from methanol increased with an increasing density of intergrowths. Also, the constraint index (defined as the relative cracking rates of n-hexane and 3-methyl pentane), which is a measure of the shape selectivity, was found to be correlated with the selectivity towards ethene. Occelli *et al.* also discuss how a few offretite intergrowths in erionite would have little effect of the shape selective properties, whereas a few percent of erionite in offretite will lead to a catalyst with essentially 8-ring properties¹¹. Additional details on the literature describing the use of offretite and related materials as catalysts in the MTH process are provided in Table S.1 of the Supplementary Information.

As is clear from the above paragraphs, offretite is commonly intergrown with erionite and this affects the shape selective properties. Thus, an important part of this work has been to synthesize phase pure materials and to investigate the accessibility to the internal pore volume, in order to be able to investigate exclusively the influence of crystal morphology on product selectivity and catalyst lifetime. Herein, we describe the preparation, characterization, and catalytic performance of a set of offretite samples having four distinct crystal morphologies and synthesized applying different strategies. We find that three of the catalysts yield product spectra dominated by C₂-C₄ aliphatics, in line with previous reports. For one of the catalysts, however, a significant production of bulky aromatic products is seen, which is a manifestation of the 12R pore system of the OFF topology. This constitutes the first demonstration of this behavior for an offretite catalyst. Finally, we show this particular display of shape selectivity can be ascribed to the catalyst particle morphology.

Experimental

We synthesized 4 samples of offretite with different crystal morphologies: oval (OFF-O), hexagonal (OFF-H), broccoli-like (OFF-B) and spherical (OFF-S) following the procedures described below. OFF-O was obtained using a method adapted from ¹³ and ¹⁴. The precursor gel had the following batch composition: 4.8 Na₂O: 1.0 K₂O: 1.0Al₂O₃: 15.8 SiO₂: 249.5 H₂O: 1.0 TMACl. 4.31 g of sodium hydroxide (Sigma Aldrich, 98%) was dissolved in distilled 3.50 g of water, followed by addition of 6.94 g of aluminum isopropoxide (Sigma Aldrich, 98%). The mixture was stirred at 100 °C until dissolution. 7.22 g of distilled water was added before cooling the solution to room temperature. A separate solution was prepared in which 2.15 g of potassium hydroxide (Sigma Aldrich 87%), 2.23 g of sodium hydroxide (Sigma-Aldrich 98%) was dissolved in 47.07 g of distilled water. 15.80 g of fumed silica (Sigma Aldrich, particle size 0.0014 µm) was added to this solution under vigorous stirring for 30 minutes. The alumina solution was introduced to the siliceous solution with further stirring for 30 minutes. 15.68 g of distilled water was added to the solution and stirred for 30 minutes. Finally, 1.88 g of tetramethylammonium chloride was introduced while stirring for 30 minutes. The precursor gel of OFF-B sample has the following batch composition: 4.8 Na₂O: 1.0 K₂O: 1.0Al₂O₃: 15.8 SiO₂: 249.5 H₂O: 1.0 TMACl: 15.8 EG. The only difference in synthesis of OFF-B sample was addition of 16.3 g of ethylene glycol (EG; Sigma Aldrich, 99.8%) as the last step of gel preparation. The precursor solutions of OFF-O and OFF-B were transferred to Teflon liners which were placed in autoclaves and heated to 190 °C for 5 h. In the next step the autoclaves were submerged in cold water to return them to room temperature. The product was filtered and washed using distilled water and dried overnight at 110 °C. OFF-H was produced from the gel having the same gel composition like OFF-B: 4.8 Na₂O: 1.0 K₂O: 1.0Al₂O₃: 15.8 SiO₂: 249.5 H₂O: 1.0 TMACl: 15.8 EG, but 3.8 g of ethylene glycol (EG; Sigma Aldrich, 99.8%) was added to the 25 g of gel after 2 h of crystallization time at 190 °C and subsequently left for additional 3 h of crystallization. OFF-S sample was synthesized using a method adapted from ^{14, 15}. The precursor gel has the following batch composition: 6.5 Na₂O: 1.9 K₂O: Al₂O₃: 22.7 SiO₂: 252 H₂O: 0.5TMACl. 2.916 g of sodium hydroxide (Sigma Aldrich, 98%) and 1.62 g of potassium hydroxide (Sigma Aldrich, 87%) were dissolved in 15.21 g of distilled water. 1.08 g of Sodium aluminate (Riedel-de Haen, Al₂O₃:50-56%) was added and the mixture stirred until dissolution. 22.36 g of colloidal silica (Sigma Aldrich, Ludox HS-40) was added to this solution with vigorous stirring. 0.67 g of tetramethylammonium chloride (Sigma Aldrich, 97%) was added under stirring. The precursor solution was transferred to a Teflon lined autoclave and heated to 100 °C for eight days. The autoclave was then submerged in cold water to return it to room temperature and quench the reaction. The product was filtered and washed using distilled water and dried overnight at 110 °C.

Zeolite Characterization

Offretite samples were characterized by: powder X-ray diffraction (XRD), Single crystal X-ray diffraction (SC-XRD), scanning electron microscopy (SEM), energy dispersive X-ray spectroscopy (EDS), gas-volumetric nitrogen sorption experiments and microgravimetric benzene adsorption. XRD patterns were collected on a Philips XPertPro (CuK α) using Bragg-Brentano geometry. The size, morphology, and Si/Al ratio were determined with scanning electron microscopy. Micrographs were recorded on FEI Quanta 200 FEG-ESEM equipped with an Everhart-Thornley detector and EDAX EDS detector. Single crystal X-ray diffraction experiments were carried out at beamline I911-3 at the MAX2 synchrotron at MaxLab, Lund ¹⁶, working with $\lambda = 0.760 \text{ \AA}$. The measurements were carried out at 100 K, on four separate crystals. The data were refined using the olex2.refine refinement package¹⁷. The BET specific surface area (SSA) and pore volume were determined by nitrogen physisorption measurements at liquid nitrogen temperature (in a range of relative pressure 0–0.99 p/p_0) on a Belsorp-mini II instrument. The sample was outgassed under vacuum for 5 h; 1 h at 80 °C, and 4 h at 300 °C before the measurement.

Microgravimetric benzene adsorption isotherms were measured with an intelligent gravimetric analyzer (IGA-002, Hiden Analytical), based on an ultrahigh-vacuum (UHV) microbalance (weighing resolution of 0.2 mg) with integrated temperature and pressure control. Temperature control was based on a thermostated water bath/circulator, while pressure control was achieved with a Baratron capacitance manometer (accuracy 0.05 mbar). The samples were placed in a pan and activated by heating at 450 °C for 6 h in the vacuum of the order 10^{-3} mbar. After cooling the system to 25 °C the vapors of benzene were introduced by an operation valve and the adsorption isotherms were measured varying the benzene equilibrium pressure in the range of 0–80 mbar.

Uptake simulations were performed in Accelrys Materials Studio version 8.1. Simulation of a geometry optimized benzene molecule as the adsorptive were performed at temperature of 298 K using four unit cells of the OFF structure as an adsorbent. The Metropolis method and COMPASS force field were adopted. Simulations were performed over a pressure range of 0.0001–100 kPa, in which 50 fugacity steps were distributed logarithmically so that there were more data points in the steep initial portion of the isotherm. The “Fine” quality setting (involving 100,000 equilibration steps and 1,000,000 production steps) was used for all simulations. Charges were force field assigned. Electrostatic forces were calculated with the Ewald method while van der Waals forces were calculated atom based. No constraints were assigned. Due to the statistical nature of the calculations, the isotherms (very) slightly differed when simulations were repeated.

The crystal shape was simulated using the Bravais-Friedel Donnay-Harker (BFDH) method as implemented in Materials Studio 8.1. The BFDH method allows the estimation of the morphology from the crystal symmetry and the lattice parameters without taking into account the chemical nature and packing of the atoms or molecules that form the crystal (Figure 1a).

FT-IR spectra were collected using a Bruker Vertex70 instrument equipped with a Harrick Praying Mantis accessory, able to collect data in Diffuse Reflectance mode (DRIFT). 128 spectra were averaged for each acquisition with a spectral resolution of 2 cm^{-1} . Data are reported in Log(R) vs. Wavenumber. The samples were activated in a 15 $\text{ml}\cdot\text{min}^{-1}$ He flow from RT to 450 °C (5 °C $\cdot\text{min}^{-1}$) in order to remove water, then cooled down to 120 °C to dose vapors of deuterated acetonitrile (CD₃CN, supplied by Sigma-Aldrich) through a 15 $\text{ml}\cdot\text{min}^{-1}$ He flow as probe molecule. The desorption of the probe was performed fluxing pure He (at the same conditions) for approximately 15 hours. The temperature was maintained at 120 °C in order to limit, either contamination by moisture (observed below 100 °C) and isotopic exchange occurring between the

deuterium of CD₃CN and the protons of the zeolites (observed above 150 °C). CD₃CN has been used instead of CH₃-CN to avoid the well-known spectroscopic complication due to Fermi resonance between the $\nu(\text{CN})$ vibration and the combination mode $\delta(\text{CH}_3) + \nu(\text{CC})$.¹⁸

Catalytic testing

Offretite samples were tested as acid catalysts in the Methanol to Hydrocarbons reaction (MTH) at 400 °C using a U-shaped fix bed quartz reactor (i.d. 7 mm). The catalyst powders were pressed, crushed and sieved, so that, only particles between 250 and 420 μm were used in the catalytic test. In each reaction, 100 mg of catalyst were used and calcined in situ at a temperature of 550 °C for 1 h using a pure flow of oxygen. Methanol was fed by flowing He through a saturator resulting in a partial pressure of 130 mbar, giving rise a WHSV of 2g MeOH gcat⁻¹ h⁻¹. The purpose of calcining the samples in situ was to remove all possible species adsorbed during the previous catalyst handling steps. The products of the reaction were analyzed by an online gas chromatograph connected to the outlet of the reactor using a heated transfer line. An Agilent 6890A equipped with FID and an Agilent J&W capillary column (length 60 m, 0.530 mm i.d., stationary phase thickness of 20 μm) were used. The temperature program was set from 45 °C to 260 °C with a heating rate of 25 °C min⁻¹ and hold times of 5 minutes and 11 minutes at the beginning and the end of the ramp respectively.

Results and discussion

Morphology of offretite crystals

PXRD patterns of the four OFF samples (**Figure 2**) confirmed that they were either phase pure or almost phase pure OFF including small amount of analcime (ANA), which appeared in the samples crystallized with an addition of ethylene glycol as growth modifier (OFF-B and OFF-H).

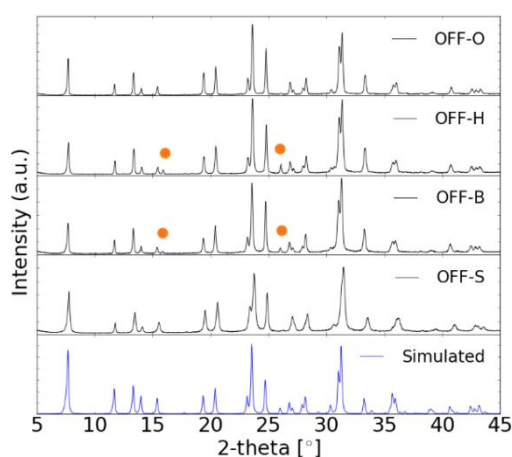


Figure 2. Observed and simulated (bottom) powder XRD patterns of the four OFF samples. The orange dots indicate small impurities of the dense analcime (ANA) phase.

The sample names introduced in the experimental section, oval (OFF-O), hexagonal (OFF-H), broccoli-like (OFF-B) and spherical (OFF-S); reflect the observed morphologies (See **Figure 3** and **Figure 4**). **Table 1** presents an overview of average particle dimensions and aspect ratios, as well as the elemental composition. The OFF-O and OFF-H have similar morphology and size (**Figure 3 a,c**). However, all the OFF-H crystal faces are distinct and smooth whereas the ones of OFF-O are rough and not very well defined. For the OFF-H sample, the crystals are more well-defined and appear to be nearly perfectly hexagonal. Similarly to OFF-H, a terminal view on the (001) surfaces of the OFF-O crystals shows a hexagon facet (**Figure 4a**), but this surface is more faulted and appears to be formed of many connected micro-crystals (**Figure 4b**). This appearance has been commented on in the literature ¹⁹, raising a question if offretite of this morphology forms actual single crystals or rather an agglomerates or bundles of separated single crystals. This issue will be resolved below. The OFF-B crystals have a double-ended broccoli-like shape (**Figure 3b**) which consist of flared tips (**Figure 4c**) and a central shaft (**Figure 4d**). The crystals are around 23 μm long, 8 μm across the narrow shaft and 15 μm across the widest point of the flared tips. The endings appear to form highly ordered closely packed, hexagonal columns. OFF-S has similar micro-crystalline structure to OFF-O, however the crystals differ significantly in size, and their morphology is more spherical (**Table 1**).

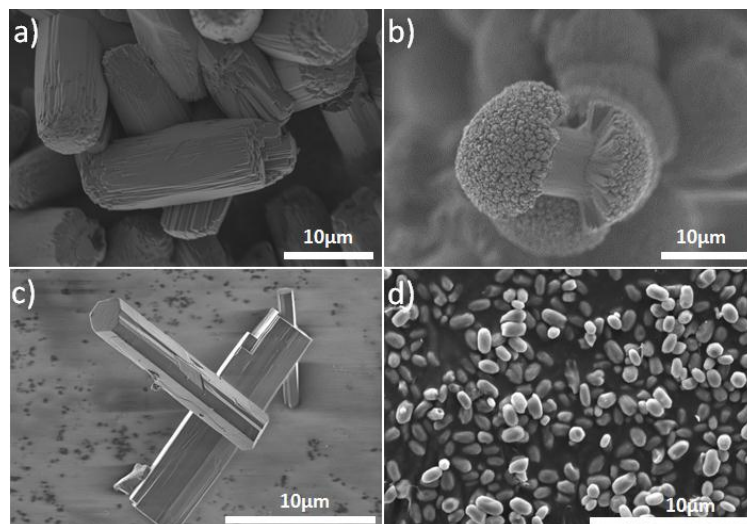


Figure 3. Scanning electron micrographs at the same magnification of (a) oval shaped offretite (OFF-O); (b) broccoli-like shaped offretite (OFF-B); (c) hexagonal offretite crystals (OFF-H), (d) Spherical offretite crystals (OFF-S).

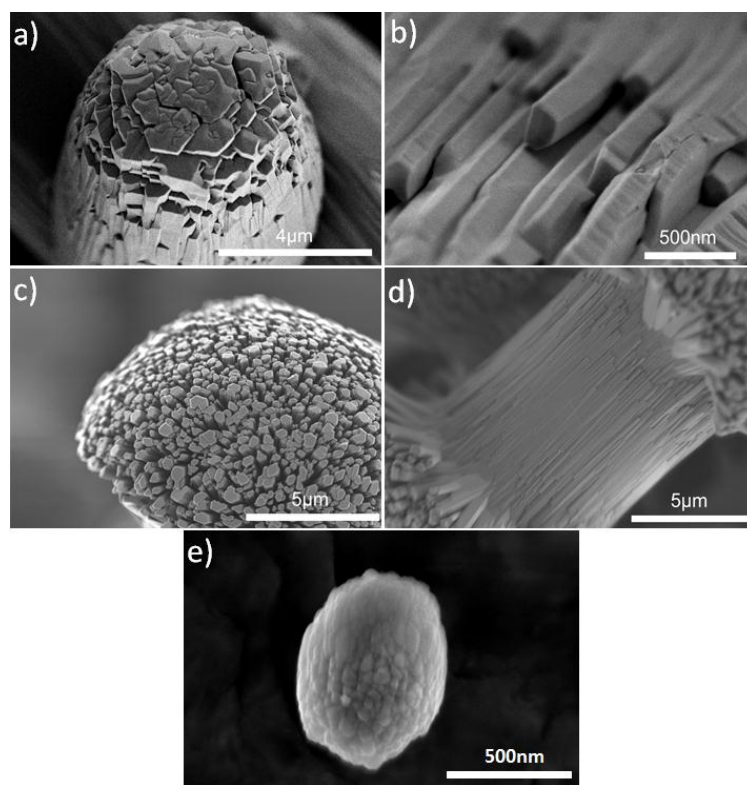


Figure 4. Scanning electron micrographs presenting details: a) Terminal view of OFF-O crystal with imperfect hexagon (001) facet; b) The lateral part the OFF-O crystal formed by many connected micro-crystals elongated in the c direction ; c) The tip of OFF-B crystal forming an agglomeration of highly ordered, closely packed, hexagonal columns; d) The central shaft of OFF-B crystal that, in a way similar to the OFF-O crystals, consists of closely packed micro-crystals elongated in the c direction; e) Detail showing that the OFF-S crystal has similar micro-structure as OFF-O.

Table 1. Average particle diameters for the offretite crystals with standard deviations. The Si/Al ratios were detected with EDS.

Sample name	Morphology	Average length [μm]	Average width [μm]	Average aspect ratio [μm]	Si/Al
OFF-O	Oval	17±3	6±1	3	3.6
OFF-H	Hexagonal	17±2	5±2	3	2.6
OFF-B	Broccoli-like	23±2	8.4±0.6	3	2.5
OFF-S	Spherical	1.1±0.4	1.0±0.2	1.1	4.6

It is instructive to compare the observed morphologies (**Figure 3** and **Figure 4**) to the idealized simulated morphology (**Figure 1a**). According to the BFDH method, the crystal morphology is determined by the slow-growing faces. The resulting model morphology is perfectly hexagonal as shown in **Figure 1a**. This result is in relatively good agreement with the appearance of the OFF-O and OFF-H crystals. This may indicate that the growth of the OFF-O and OFF-H crystals is controlled by thermodynamic effects, with kinetic factors playing a secondary role in the determination of the crystal morphology. The crystal morphology is very sensitive to synthesis conditions, and these are not taken into account for the BFDH simulation, which are based only on the crystal symmetry and the lattice parameters. Thus the interesting morphology of the OFF-B sample cannot be explained by this method. Offretite crystals with similar morphology have already been discussed in the literature, and they are referred to by a variety of names, such as wheat sheaf, peanut or dumbbell-like morphology. Lillerud and Reader¹³ observed that changes in the Si/Al ratio of offretite and variation in synthesis temperature of zeolite T lead to the production of crystals with similar habit. This particular morphology has also been observed for different types of materials such as metal carbonates²⁰, oxalates, oxides²¹, nanoparticles²², and others^{23, 24}.

The key differences in the synthesis of spherical crystals of OFF-S (**Figure 4e**) were the types of silica and aluminum sources, a decreased amount of water, a lower temperature, and an extension of the crystallization time. The longer crystallization period (8 days) was required because the colloidal silica source had first to depolymerize at 100 °C before the crystallization started. A lower level of water in the synthesis gel indicates that even though the cation levels were similar to the other synthesis procedures, the gel produced in this system was more alkaline¹⁴. Higher pH of the precursor gel improved solubility of the silica and aluminum sources. As a consequence, the nucleation rate increased providing small crystals. The addition of ethylene glycol, both before crystallization at 190°C (OFF-B) and after 2 h of crystallization (OFF-H) lead to synthesis of product with slightly lower Si/Al ratio (**Table 1**).

Table 2 presents results from N₂ adsorption. Full isotherms are shown in the supplementary information. All samples yield type I isotherms, as expected for microporous materials. All four samples display high specific surface areas and micro pore volumes, indicative of well crystalline samples.

Table 2. Results of volumetric N₂ adsorption measurements.

Sample name	S_{BET} (m ² /g)	S_{ext} (m ² /g)	V_{micro} (cm ³ /g)	V_{meso} (cm ³ /g)
OFF-O	602	2	0.24	0.01
OFF-H	534	6	0.21	0.03
OFF-B	519	4	0.20	0.02
OSS-S	604	18	0.25	0.05

Acidity characterization by FT-IR Spectroscopy

Infrared spectroscopy enables to directly observe hydroxyl groups associated with zeolite acidity, thus the technique was applied to characterize acidic properties of the offretite samples. Crystals having similar size to the wavelength of the mid-IR light (OFF-O, OFF-B, and OFF-H) give rise to scattering of the IR radiation observed across all the spectral range of interest. In consequence, no information about acid sites can be obtained from the spectra recorded in transmission mode. To overcome the limitation, the experiments were conducted using Diffuse Reflectance Infrared Fourier Transform (DRIFT) technique, which is a surface sensitive method and causes less scattering losses than measurements performed in transmission mode. Deuterated acetonitrile (CD₃CN) was applied as probe molecule thanks to its sufficiently high interaction energy even at temperatures higher than room temperature (see the experimental section). When CD₃CN interacts with Lewis and Brønsted acid sites, both the zeolite hydroxyl groups and the acetonitrile $\nu(\text{CN})$ frequency will shift³⁰.

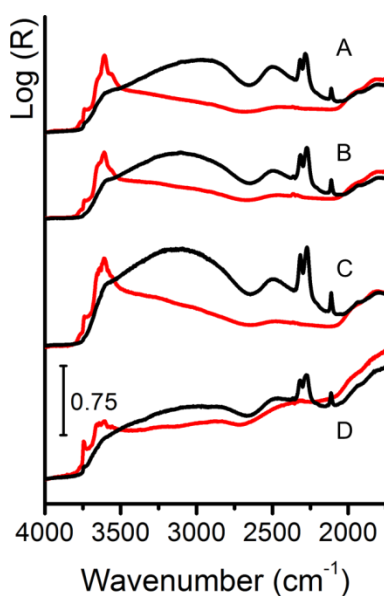


Figure 5. DRIFT spectra of oval shaped offretite (OFF-O, part A), hexagonal offretite crystals (OFF-H, part B), broccoli-like shaped offretite (OFF-B, part C) and spherical offretite crystals (OFF-S, part D). Red curves represent the sample at 120 °C after activation in He, while black curves represent the maximum coverage of CD₃CN on the samples (θ_{MAX}).

Figure 5 shows the DRIFT spectra of the samples at 120 °C after activation in He, before dosing the probe molecule (red curves) and at θ_{MAX} (black curves) of CD₃CN. The spectra obtained in case of the activated samples (red curves) show strong similarities. In fact all are characterized by: i) an absorption centered at 3740 cm⁻¹, assigned to hydroxyl group belonging to isolated external SiOH; ii) a more intense complex band, with at least three components in the range expected for the strong Al(OH)Si Brønsted acid sites;^{26, 28, 31} iii) a broad absorption extending till about 2000 cm⁻¹, testifying the presence of extensive strong hydrogen bonding that could involve both defective species and the persistence of entrapped moisture molecules. The complex band associated to the strong Brønsted acidic sites is very intense in all the samples, due the high Al content (Si/Al ranging from 2.5 to 4.6). As previously described,^{26, 28, 31} offretite shows some similarities with the faujasite topology, having Brønsted acid sites slightly less acidic (component at 3660 cm⁻¹) and hydroxyls species associated to hexagonal prisms, that originate a component at lower frequency, as they are interacting with neighbors oxygen. A third component at 3605 cm⁻¹ is clearly visible in all the samples.^{26, 28, 31} With respect to the band ascribed to the isolated silanols, we note that it is definitely more intense in the case of the OFF-S sample, as expected for the zeolite characterized by smaller particles size distribution.

When CD₃CN interacts with the samples the infrared spectra change substantially. First of all, both silanols and strong Brønsted acidic sites are eroded giving rise to a complex spectrum extending at lower frequency and characterized by the well-known shape with the presence of two broad pseudo bands separated by a minimum (A and B following refs. 27, 29, 30). A third component (labeled C) falls out of the spectral range reported. This effect is normally associated with the formation of hydrogen bonds of medium to strong intensity. The formation of hydrogen bonded adducts between the hydroxyls and the CD₃CN, occurs through the interaction with the CN group, as testified by the growth of new components blue-shifted with respect to the frequency of the physisorbed acetonitrile (2265 cm⁻¹).^{18, 27, 29, 30} In particular we observe a maximum at 2315 cm⁻¹ and a more complex band with at least two components (2282 and 2272 cm⁻¹) (Figure 4. in supplementary information). As the experiments were performed keeping the sample at 120 °C, in order to limit the moisture contamination, we do not observe any physisorbed counterpart. The very high frequency band has been associated to the interaction with strong Lewis sites, while the less perturbed components can be associated to hydroxyls with different acidities.

Figure 6 presents the methanol conversion at 400 °C versus time on stream for the four catalysts samples with different crystal shape. The $t_{1/2}$ values (vertical dotted line) are the times needed to reach 50 % conversion. In line with the previous reports summarized in the introduction, rapid deactivation is observed for all catalysts. The OFF-O and OFF-H samples, which have similar aspect ratios and size display virtually identical lifetimes. The OFF-B catalyst has approximately a doubled lifetime, despite the similar overall crystal dimensions. It is perhaps not surprising that the longest catalyst life time is observed for the OFF-S, having comparatively very small crystals. The $t_{1/2}$ is more than four times higher than the value found for the samples that deactivate the fastest. Generally, small crystal dimensions are associated with long catalyst lifetimes^{1, 32, 33}. It is harder to rationalize the intermediate performance of the OFF-B catalyst, but it might be that the small branched hexagonal crystals that comprise the 'broccoli' surface leads to an extension of the lifetime after deactivation of the central part of the crystal. This could then explain the improved catalytic performance compared to OFF-O and OFF-H.

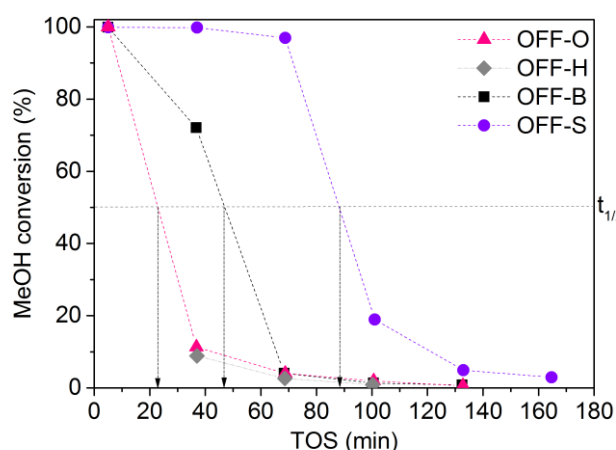


Figure 6. Methanol conversion versus time on stream at 400 °C and WHSV=2 gMeOHgcatalyst-1h-1 for offretite catalysts with different morphology.

Figure 7 shows the product selectivities for all the offretite catalysts at the same MeOH conversion level (100%). Because of the rapid deactivation, product selectivities could only be compared at full conversion. It may be noted, however, that the product selectivities were relatively unchanged for the period of (nearly) full conversion seen for OFF-S. The offretite samples possessing similar morphology, OFF-O and OFF-H, not only show almost the same catalytic lifetime, but also the product distribution is very similar. For the OFF-B sample, a slight increase in the heavier product fractions, in comparison to OFF-O and OFF-H, is seen. However, the product distribution seen for the spherical crystals, OFF-S, is clearly shifted towards the C₅₊ product fraction. Overall, the OFF-O, H, and B catalysts yield a product spectrum rich in C₂ and C₃ aliphatics in line with previous reports. The results for OFF-S, however, differ substantially. Occelli¹¹ reports that the highest yield of ethene (45-50 C%) was seen for highly intergrown catalysts, and that the maximum ethene yield was 27 C% for an offretite catalyst prepared using tetramethylammonium having morphology similar to OFF-S. However, the substantial yield of C₅₊ and aromatics (see below) seen here appears to be unprecedented, even for non-intergrown offretite.

A more detailed analysis of these heavier products is presented in **Figure 8**. Clearly, not only does OFF-S produce more of the heavy products, but the analysis of the aromatics distribution reveals that OFF-S is selective towards bulkier products that were not observed at all for any of the other catalysts, e.g. penta- and hexamethylbenzene (**Figure 8**). Penta- and hexamethylbenzene are typical MTH products for 12 ring zeolite catalysts such as mordenite and zeolite beta. Typically, for zeolite beta, hexaMB is in excess, whereas for mordenite, the hexaMB to pentaMB is often smaller than 1 ^{34,35} as seen for OFF-S here.

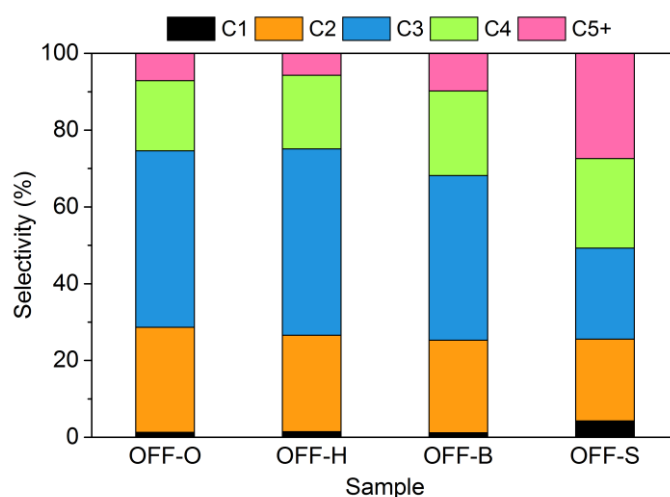


Figure 7. Product selectivity for the different offretite samples at 100 % MeOH conversion.

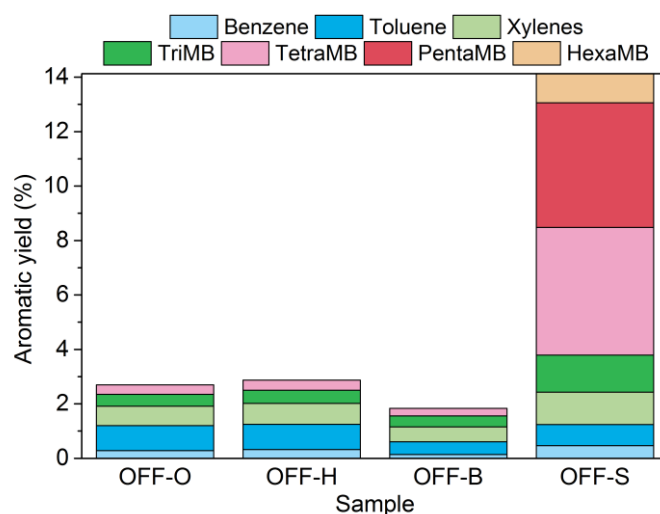


Figure 8. Aromatics distribution of four offretite samples.

Twinning mechanisms – is the pore volume accessible?

In the previous section, substantial variations in catalyst performance among the samples were documented. In particular, it was revealed that the product selectivity observed for OFF-S differs significantly from those of the other catalysts. The remainder of this manuscript will be dedicated to elucidation of the cause of this unusual behavior, starting with an analysis of the microstructure of the samples.

OFF belongs to the ABC-6 ring family of zeolite topologies (**Figure 9**), and is known to form stacking faults as observed in the OFF-ERI stacking disordered series. A single fault of this type will lead to two twin domains of OFF with a twin law corresponding to a 180-degree rotation around the unique c-axis. Importantly, such faults lead to a blocking of the main 12-ring channel (**Figure 9c**). Single crystal X-ray diffraction was performed on 4 different OFF crystals. Two of these were picked from the OFF-O sample, whereas two more were picked from a sample of hexagonal crystals very similar to OFF-H, but prepared in a slightly different manner (see supplementary information for details). A lattice of well-defined Bragg spots was observed for all the OFF-O and hexagonal crystals. This proves that the OFF-O particles are single crystals, despite the substantial surface structure seen with SEM (**Figure 3 Figure 4**). In case of OFF-B, weak Debye-Scherrer rings were observed in addition to the sharp Bragg spots. The powder rings are presumably caused by diffraction from the crystallites in the branching part, whereas the shaft diffracts like a single crystal. This shows, not surprisingly, that the OFF-B particles are polycrystalline. The OFF-S crystals were too small for the single crystal analysis. The primary objective of the single crystal diffraction was not to determine the crystal structure (which obviously is known), but rather to analyze the degree of twinning. .cif files are available in the supplementary information.

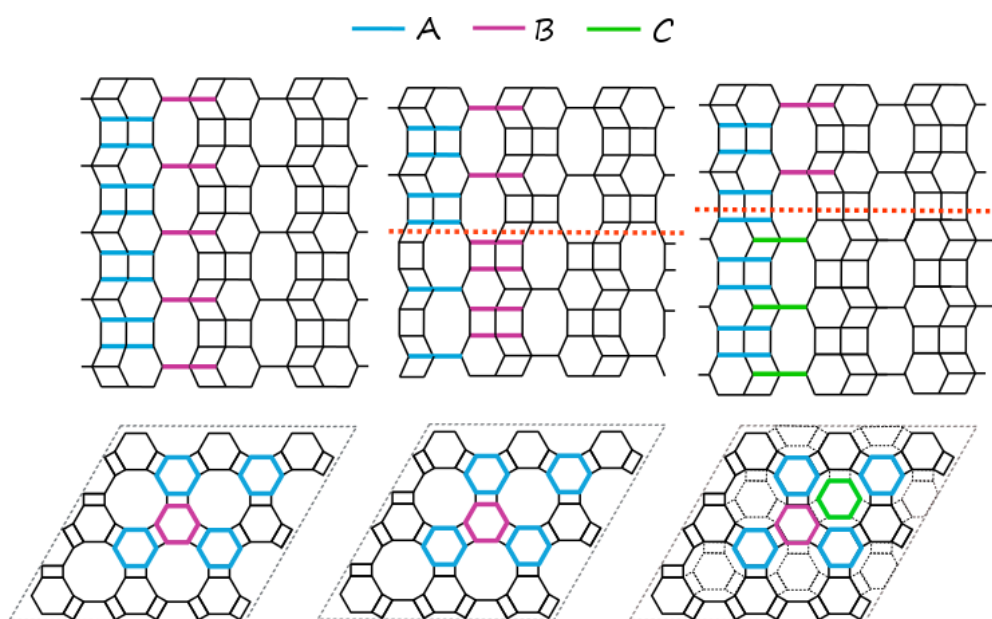


Figure 9. [100] (top row) and [001] (bottom row) projection of offretite framework. (Left column) The layer sequence AABAAB of offretite without twinning (ideal structure). (Middle column) proposed stacking fault leading to two twin domains without blocking the 12 ring channel; (right column) a stacking fault of the type known from OFF- ERI stacking disordered materials leading to two twin domains and a blocked 12 ring channels.

Symmetry analysis of the observed Bragg spots revealed higher symmetry than what is expected for OFF (space group: $P-6m2$). Further analysis revealed that the observed higher symmetry is a result of merohedral

twinning and that the two twin domains are related by a twin law corresponding to a 180-degree rotation around the unique c-axis. The observed twinning is therefore consistent with both types of stacking faults shown in **Figure 9**. It is well known that the stacking faults in the OFF-ERI series are randomly distributed. It has been shown that the powder diffraction data can be simulated by assuming a simple probability for the occurrence of a fault at the transition from one layer to the next ³⁶. At 0 % probability, pure OFF is observed (green curve in **Figure 10**) and at 100 % probability pure ERI is observed (red curve in **Figure 10**).

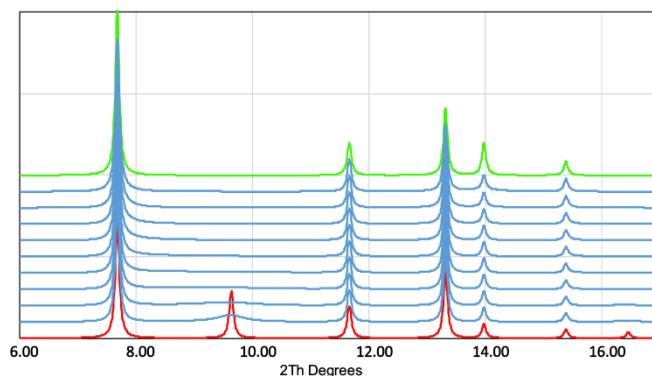


Figure 10. The simulated powder patterns of the ERI-OFF series in steps of 10% intergrowth. The patterns were simulated using DIFFAX ³⁷

The observed twin fractions were indistinguishable from 50/50 in all four cases (OFF-O: 0.7+/-0.5 and 0.6+/-0.2; hexagonal: 0.7+/-0.2 and 0.6+/-0.4).). In a case where the probability of faulting is slightly above 0%, leading to just one or two twins, it is very unlikely that a 50/50 twin fraction would be observed for all crystals; given the random nature of the faulting. This corresponds to the leftmost situation in **Figure 11**, and this scenario can effectively be ruled out. At higher densities of faults (**Figure 11** middle), it becomes increasingly likely to obtain a 50/50 twin fraction, as is observed. However, at very high fault densities (**Figure 11** right), the crystal eventually becomes disordered, leading to anisotropic peak broadening and diffuse scattering in the XRD data. This scenario will be evaluated in the next paragraphs.

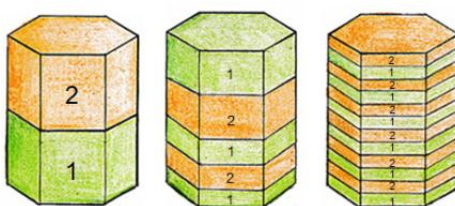


Figure 11. Schematic showing three different distributions of twin fractions (indicated by different colors) within a single crystal. In all three cases the twin fraction is 50/50, but the twinning probability is very low (left), intermediate (middle) and high (right).

At first glance there is no evidence of disorder in the observed XRD data. A simple LeBail fit results in a good fit between the model and the observed data, with no evidence of anisotropic peak broadening or diffuse scattering (**Figure 12**, left panel).

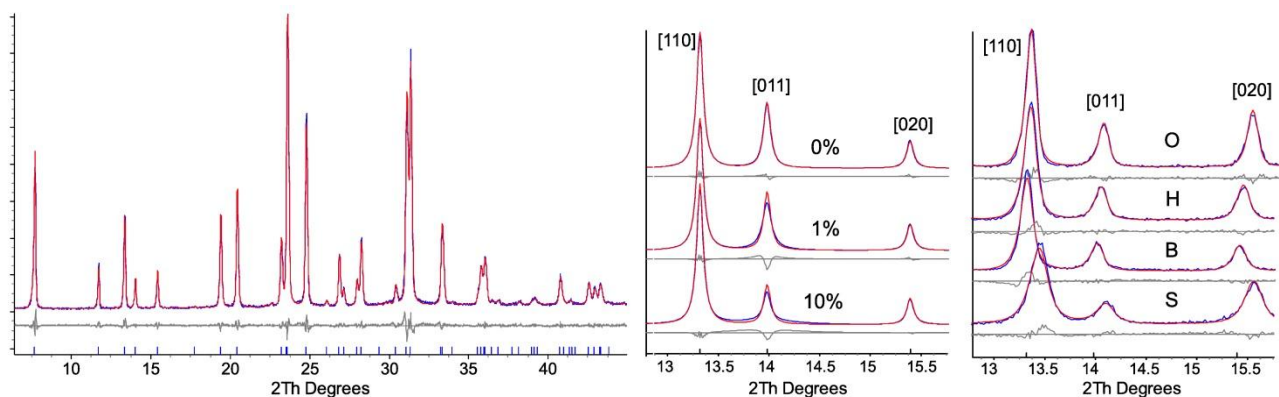


Figure 12. LeBail fit of experimental data (left) showing no anisotropic peak broadening. Full profile fit (performed in TOPAS) of the simulated data containing 0%, 1% and 10% stacking faults (middle). Full profile fit of the four OFF samples showing no evidence of stacking faults (right). Black curves correspond to simulated (middle) or observed data (right). Red and grey curves are the model and the difference curves respectively.

Closer inspection of the [011] reflection, which is the reflection showing most changes at low concentrations of stacking faults (**Figure 12**, middle panel), reveals no evidence for stacking disorder in the observed data (**Figure 12**, right panel). From this analysis it can be concluded that if stacking faults of the OFF-ERI type (**Figure 9c**) are present, they occur with a probability well below 1 %, ruling out the case illustrated in the right panel of **Figure 11**. It may be noted that a probability of say 0.1 % would correspond to 10-100 faults in a 10 μm crystal.

An OFF material described by the stacking sequence ...AABAAB... will have the 12-ring channel at the C position. Introducing a fault of the OFF-ERI type will result in the stacking sequence ...AABAABAACAAC... creating an OFF twin component with the 12-ring channel at the A position. The result of the stacking fault is that the 12-ring channels existing on both sides of the fault will be blocked by a 6-ring (**Figure 9c**). For the samples in this study, it has been established that at least a few faults exist in each crystallite as illustrated in **Figure 11**, middle panel. A consequence is therefore that large parts of the 12-ring channel system would be cut off from contributing to the MTH process.

To determine the actual fraction of the sample volume with isolated 12-ring channels, benzene uptake experiments were performed. Given that the kinetic diameter of benzene (approximately 5.9 \AA ³⁸ is substantially larger than the 8MR channels (3.6 x 4.9 \AA), it is safe to assume that benzene can penetrate into the crystals only through the pores with 12MR windows (6.7 x 6.8 \AA). As explained previously, erionite type twinning (**Figure 9**, right panel) will effectively block these large channels, whereas the proposed new twinning mechanism (or the absence of twinning altogether) would leave the 12MR channels fully accessible to the benzene molecules. **Table 3** lists the total benzene adsorption capacity for the samples (Full isotherms are provided in the supplementary information) together with the theoretical uptake value from grand canonical Monte Carlo simulations. Clearly, all four samples show a total uptake capacity which is similar or exceeds the value obtained from simulation. This essentially proves that the internal void of all four catalyst samples is fully accessible to benzene. This, in turn, can only occur if the materials have the ideal OFF structure, or are twinned according to the middle mechanism in **Figure 9**. **Table 3** also lists the benzene uptake normalized to the BET surface rather than catalyst mass. Given the similar N_2 adsorption characteristics, this normalization does not shed further light on the analysis.

Table 3. Thermogravimetric benzene uptake.

Sample name	Uptake	
	$\mu\text{mol/g}$	$\mu\text{mol/m}^2$
OFF-O	2.9	4.7
OFF-H	2.5	4.7
OFF-B	2.1	4.0
OFF-S	2.5	4.1
calculated	2.1	-

It should be kept in mind that the twinning is only actually demonstrated for the OFF-O sample and the hexagonal sample. It should also be noted that only a few (more than a single) stacking fault blocking the 12MR channels would dramatically reduce the uptake capacity, implying that this method provides a very sensitive assessment of the accessibility of the pore systems. Zhou et al.³⁹ have compiled cyclohexane adsorption abilities for several relevant materials and report a comparatively high uptake (7.8%) for OFF and substantially lower for ERI (1.0%) and zeolite T (0.8%), whereas all three materials displayed very similar adsorption amounts of n-hexane (8.8, 6.5, and 6.6%, respectively). This lends strong support to the interpretation of the present data as discussed above.

Discussion

In the preceding paragraphs, it has been demonstrated using XRD and benzene uptake measurements that the majority of the internal pore volume is accessible for all four materials under study. This indicates that the concentrations of ERI type faults (or other defects that might block the 12 ring channels) are negligible, and that the twinning observed with single crystal XRD is rather due to a type of stacking fault which does not block the 12 ring channel (**Figure 9**, middle panel). The basic characterization (nitrogen surface area, elemental analysis) indicate that any differences that might be related to these properties can be expected to be negligible. The spectroscopic characterization showed that all the samples exhibit the same types of acidic sites (silanols and strong Bronsted sites). Moreover, the larger amount of silanols observed in case of OFF-S is fully compatible with the smaller dimension of the particles. Importantly, the details provided in Table S.1 confirm that the acid site density of the materials investigated here are within the range of the materials previously employed as catalysts for the MTH reaction. Thus, we are now in a position to evaluate the differences in catalyst performance among the four samples according primarily to crystal morphology.

Figure 13 shows the product selectivities observed for the four catalysts were compared to selectivities of two relevant frameworks: CHA with 3-D 8MR pore system and MOR having 1-D 12 member-ring channels (see supplementary information for details about the pore systems and crystal morphology). Thus, one could

argue that the CHA topology should display shape selectivity similar to erionite, whereas mordenite should mimic defect free offretite. As is evident from **Figure 13**, it is clear that the selectivities observed for OFF-O, OFF-H, and OFF-B samples are very similar to SAPO-34, whereas the OFF-S catalyst is comparable to mordenite. So, despite the accessibility of the 12 ring channel system (as probed by the benzene uptake), three of the catalysts display shape selective properties usually associated with 8 ring systems. However, the OFF-S catalyst does behave as one would expect for a 12 ring topology.

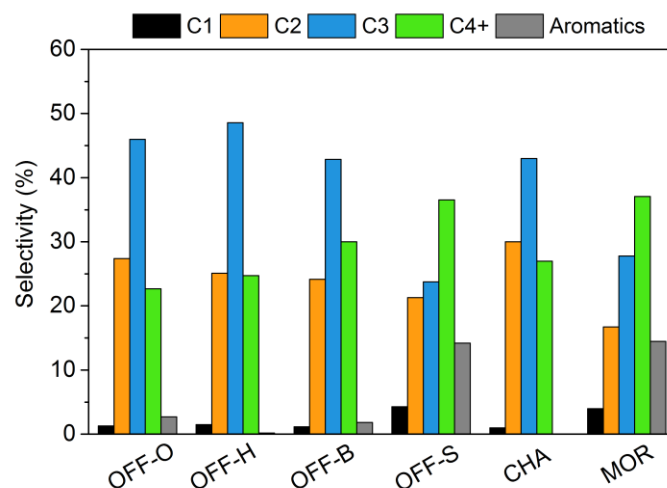


Figure 13. Comparison of product selectivities of four offretite catalysts to CHA (3-dimensional 8MR), and MOR (1-dimensional 12MR)

It is tempting to analyze the shape selective properties outlined above according to the morphology of the catalysts. To this end, **Figure 14** was created. By idealizing and simplifying the shapes of the crystals as observed with SEM, it is possible to make a rough estimate of the ratio of the facets where the 12MR channels are terminated and the facets where the 8MR channels are terminated (S_{12}/S_8). The argument is then that a high ratio of 12MR to 8MR facets should be linked to a high selectivity towards heavier products. As shown in **Figure 14**, the crystals of OFF-S, OFF-H and OFF-O are represented by hexagonal prisms with different aspect ratios. The OFF-B crystals are considered to be built of a cylinder (the core) and two hemispheres. The calculations are based on the measured crystal sizes (**Table 1**) and more details are provided in SI. As the crystal size of OFF-S differs significantly from the other samples, it is magnified to show both the idealized shape and the actual dimensions. As might be expected from the similarities in size and shape, the OFF-H and OFF-O catalysts have the lowest amount of 12MR pore openings ($S_{12}/S_8 = 0.15$). One could argue that this is reflected by their similar product distribution. Further, it is found that the OFF-B crystals have a substantially greater degree of exposure of the 12MR openings ($S_{12}/S_8 = 1.6$). However, this is not reflected by the experimental selectivities; the selectivity towards C_{5+} products is virtually the same as for the OFF-H and OFF-O catalysts. It is worth pointing out that the hemispheres of OFF-B are composed of agglomerated hexagonal crystals with aspect ratio around 4, and the degree to which any voids in between these units (which would expose 8MR openings) are accessible is unknown.

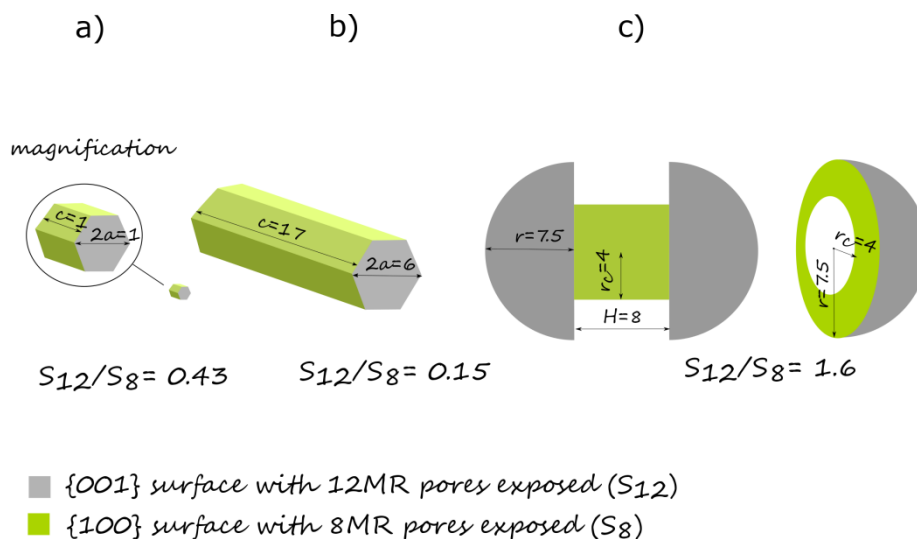


Figure 14. Qualitative model of idealized and simplified shapes of synthesized crystals: (a) OFF-S (b) OFF-O and OFF-H (c) OFF-B, which roughly estimate a contribution of 12MR and 8MR openings (S_{12}/S_8).

Finally, the experiment showed that OFF-S ($S_{12}/S_8 = 0.43$) produced the largest C_{5+} fraction. A comment should be made regarding the estimate made for OFF-S, which is now based on a hexagonal crystal shape. However, inspection of the SEM images (**Figure 3**, **Figure 4**) the crystals do appear to be quite rounded. Obviously, for the limit of a perfectly spherical crystal, the entire crystal surface would be terminated by both 8MR and 12MR channels, giving rise to an even higher S_{12}/S_8 ratio. It is clear that this simple geometrical analysis does not fully capture all relevant effects. Clearly, crystal size is another relevant parameter. We argue that a hypothetical catalyst having a morphology comprising hexagonal plates (rightmost element in Figure 1), thus having a very high S_{12}/S_8 ratio, might lead to an even more pronounced 12MR behavior. However, to prepare such a material would pose a considerable crystal engineering challenge, as such a morphology is exactly the opposite of that preferred for this crystal structure.

With respect to the literature data describing the catalyst performance of offretite and related materials summarized in the introduction and elaborated in Table S.1, there is generally little information about crystal morphology available. When data are available, the catalysts are usually rod shaped or hexagonal and micron sized. However, the TMA-offretite material studied in references 10-12 display a morphology and size quite similar to the OFF-S sample studied here, but without yielding significant amounts of C_{5+} hydrocarbons from methanol. The range of acid site densities (Si/Al) examined in the literature ranges from 3.3 to 5.8 (from elemental analysis) or up to 9.2 as determined by ^{29}Si NMR. It should be emphasized that despite this range in acid site densities found among the catalysts tested in the literature, all of them display shape selective properties primarily associated with an 8MR pore system.

To summarize, the four offretite catalysts display significant differences in both catalyst lifetime and product selectivities. The selectivities observed for the OFF-S catalyst actually reflects the 12MR channels of the structure, in contrast to the other samples studied and literature reports, which invariably display a typical 8MR shape selectivity, despite the presence of accessible 12MR channels. This constitutes an example of morphology induced shape selectivity: for OFF-H and OFF-O, the 8MR channels overshadow the effects of the 12MR channels, due to their much greater exposure at the external crystal surfaces and this gives rise to a typical 8MR product spectrum, similar to CHA. It is the morphology of the crystals that govern the relative contribution of the two pore systems to the observed product shape selectivity. For OFF-B, the situation is

more complex. The broccoli-like crystal shape is hard to analyze according to surface exposure, and it is likely that crystal size and diffusion length also plays a role. However, for the OFF-S catalyst, the 12MR channels are exposed on the entire crystal surface (assuming spherical particles), which gives rise to a typical 12MR product spectrum, similar to MOR. To our knowledge, this constitutes the first report of such behavior for an offretite catalyst in the MTH reaction.

Conclusions

This report describes the preparation of four offretite catalyst samples with distinct crystal morphologies (oval, hexagonal, broccoli-like, and spherical) and fully accessible 12-ring channel systems. These materials were characterized, and their catalytic performance was evaluated in the conversion of methanol to hydrocarbons (MTH). Particular care was taken in the structural characterization and evaluation of structural defects like twinning, since these features could severely limit access to the zeolite channel system and therefore affect the catalytic properties of the materials.

Offretite strongly prefers to crystallize into hexagonal prisms, where the 8MR and 12MR channels are accessed from the side and the end of the crystals, respectively. For the relatively large OFF-O and OFF-H, the 8MR channel openings are abundant and dominate, giving rise to a typical 8MR product spectrum, despite the presence of accessible 12MR channels. This is presumably caused by the high degree of exposure of the crystal facets where the 8MR channels terminate. A similar product distribution is seen for the complex, broccoli-like crystals.

However, unlike all previous reports, the product distribution (product shape selectivity) seen for the small, spherical crystals is controlled by the 12-ring channels and reflects the actual offretite topology, in contrast to the other catalysts and previous reports. The structural studies combined with benzene uptake measurements, show that the observed twinning is of a different type observed in OFF-ERI type disordered materials, which would lead to blocking of the 12MR channels. The fact that the crystals are twinned while maintaining a fully accessible pore system constitutes a new perspective on offretite twinning. Thus, it was possible to eliminate an influence of twinning on the catalytic properties, enabling us to investigate the effect of crystal morphology on the product selectivity and catalyst life time in the MTH reaction. Taken together, the results presented here constitute a new example of morphology induced shape selectivity for zeolite catalysts.

Acknowledgements

Financial support was received via the European Industrial Doctorates project “ZeoMorph” (Grant Agreement No. 606965), part of the Marie Curie actions (FP7-PEOPLE-ITN-EID).

1. G. Yang, Y. Wei, S. Xu, J. Chen, J. Li, Z. Liu, J. Yu and R. Xu, *The Journal of Physical Chemistry C*, 2013, **117**, 8214-8222.
2. K. A. Łukaszuk, P. del Campo Huertas, A. Molino, M. Nielsen, D. Rojo-Gama, J. S. Martinez-Espin, K. P. Lillerud, U. Olsbye, S. Bordiga, P. Beato and S. Svelle, in *Nanotechnology for Energy Sustainability*, Wiley-VCH Verlag GmbH & Co. KGaA, 2017, DOI: 10.1002/9783527696109.ch1, pp. 1-40.
3. S. Teketel, L. F. Lundegaard, W. Skistad, S. M. Chavan, U. Olsbye, K. P. Lillerud, P. Beato and S. Svelle, *J. Catal.*, 2015, **327**, 22-32.
4. U. Olsbye, M. Bjørgen, S. Svelle, K.-P. Lillerud and S. Kolboe, *Catal. Today*, 2005, **106**, 108-111.
5. U. Olsbye, S. Svelle, M. Bjørgen, P. Beato, T. V. W. Janssens, F. Joensen, S. Bordiga and K. P. Lillerud, *Angew. Chem. Int. Ed.*, 2012, **51**, 5810-5831.
6. P. Dejaifve, A. Auroux, P. C. Gravelle, J. C. Védrine, Z. Gabelica and E. G. Derouane, *J. Catal.*, 1981, **70**, 123-136.
7. V. Kanazirev and T. Tsoncheva, *Can. J. Chem.*, 1992, **70**, 1997-2002.
8. B. E. Langner, *Applied Catalysis*, 1982, **2**, 289-302.
9. S. Ceckiewicz, *Journal of the Chemical Society, Faraday Transactions 1: Physical Chemistry in Condensed Phases*, 1984, **80**, 2989-2998.
10. M. W. Anderson, M. L. Occelli and J. Klinowski, *The Journal of Physical Chemistry*, 1992, **96**, 388-392.
11. M. L. Occelli, R. A. Innes, S. S. Pollack and J. V. Sanders, *Zeolites*, 1987, **7**, 265-271.
12. J. V. Sanders, M. L. Occelli, R. A. Innes and S. S. Pollack, *Stud. Surf. Sci. Catal.*, 1986, **28**, 429-436.
13. K. P. Lillerud and J. H. Raeder, *Zeolites*, 1986, **6**, 474-483.
14. A. Holmes, PhD, The University of Manchester, 2011.
15. 1972.
16. T. Ursby, J. Unge, R. Appio, D. T. Logan, F. Fredslund, C. Svensson, K. Larsson, A. Labrador and M. M. G. M. Thunnissen, *Journal of Synchrotron Radiation*, 2013, **20**, 648-653.
17. L. J. B. O. V. Dolomanov, R. J. Gildea, J. A. K. Howard and H. Puschmann, *J. Appl. Cryst.*, 2009, **42**, 339-341.
18. H. Knoezinger and H. Krietenbrink, *Journal of the Chemical Society, Faraday Transactions* 1975, **71**, 2421-2430.
19. T. E. Whyte, E. L. Wu, G. T. Kerr and P. B. Venuto, *J. Catal.*, 1971, **20**, 88-96.
20. H. Cölfen and L. Qi, *Chemistry – A European Journal*, 2001, **7**, 106-116.
21. N. Sasaki, Y. Murakami, D. Shindo and T. Sugimoto, *J. Colloid Interface Sci.*, 1999, **213**, 121-125.
22. M. K. Singh, A. Agarwal, R. Gopal, R. K. Swarnkar and R. K. Kotnala, *J. Mater. Chem.*, 2011, **21**, 11074-11079.
23. O. Prymak, V. Sokolova, T. Peitsch and M. Epple, *Crystal Growth & Design*, 2006, **6**, 498-506.
24. G.-Y. Chen, B. Dneg, G.-B. Cai, T.-K. Zhang, W.-F. Dong, W.-X. Zhang and A.-W. Xu, *The Journal of Physical Chemistry C*, 2008, **112**, 672-679.
25. S. Bordiga, C. Lamberti, F. Bonino, A. Travert and F. Thibault-Starzyk, *Chemical Society Reviews*, 2015, **44**, 7262-7341.
26. S. Ceckiewicz, *Journal of the Chemical Society-Faraday Transactions I*, 1984, **80**, 2989-2998.
27. A. V. Ivanov, G. W. Graham and M. Shelef, *Applied Catalysis B-Environmental*, 1999, **21**, 243-258.
28. C. Mirodatos, A. Aboukais, J. C. Vedrine and D. Barthomeuf, *Journal of the Chemical Society-Faraday Transactions I*, 1978, **74**, 1786-1795.
29. C. Pazè, A. Zecchina, S. Spera, G. Spano and F. Rivetti, *Physical Chemistry Chemical Physics*, 2000, **2**, 5756-5760.
30. A. G. Pelmentschikov, R. A. Vansanten, J. Janchen and E. Meijer, *Journal of Physical Chemistry*, 1993, **97**, 11071-11074.
31. E. L. Wu, T. E. Whyte and P. B. Venuto, *Journal of Catalysis*, 1971, **21**, 384-393.
32. W. Dai, G. Wu, L. Li, N. Guan and M. Hunger, *ACS Catalysis*, 2013, **3**, 588-596.

33. N. Nishiyama, M. Kawaguchi, Y. Hirota, D. Van Vu, Y. Egashira and K. Ueyama, *Applied Catalysis A: General*, 2009, **362**, 193-199.
34. M. Bjørgen, U. Olsbye, S. Svelle and S. Kolboe, *Catal. Lett.*, 2004, **93**, 37-40.
35. M. Bjørgen, U. Olsbye, D. Petersen and S. Kolboe, *J. Catal.*, 2004, **221**, 1-10.
36. www.iza-structure.org].
37. <http://www.public.asu.edu/~mtreacy/DIFFaX.html>].
38. H. Abrevaya, in *Zeolites in Industrial Separation and Catalysis*, Wiley-VCH Verlag GmbH & Co. KGaA, 2010, DOI: 10.1002/9783527629565.ch13, pp. 403-478.
39. F. Zhou, P. Tian, Z. Liu, G. Liu, F. Chang and J. Li, *Chinese Journal of Catalysis*, 2007, **28**, 817-822.